Design and field measurements of printed-circuit quadrupoles and dipoles

W. W. Zhang,* S. Bernal, H. Li, T. Godlove, R. A. Kishek, P. G. O'Shea, M. Reiser, and V. Yun
Institute For Plasma Research, University of Maryland, College Park, Maryland 20742

M. Venturini
Stanford Linear Accelerator Center, Stanford University, Stanford, California 94309
(Received 28 September 2000; published 8 December 2000)

Air-core printed-circuit (PC) quadrupoles and dipoles have been developed for the University of Maryland electron ring, currently under construction. The quadrupoles and dipoles are characterized by very small magnetic fields (about 15 G at the aperture edge) and small aspect ratios (length/diameter < 1). We review the theory behind the design of the PC lenses and bending elements, and present general expressions for estimating the values of integrated field and integrated field gradient as functions of design parameters. The new quadrupole magnet represents an improvement over an earlier version which was based on an empirical approach. Further, we summarize the results of multipole content of the magnet fields as measured with a rotating coil apparatus of special construction. The results are compared with calculations with an iron-free magnetics code and are related to different types of errors in the manufacture and assembly of the PC magnets.

PACS numbers: 41.85.Lc, 07.55.Db, 85.70.–w

I. INTRODUCTION

A compact electron ring is being developed at the University of Maryland for studies of space charge dominated beam transport [1] with potential applications to all areas where intense beams of high quality are required. The University of Maryland electron ring (UMER) is designed for the transport of a 10 keV, 100 mA, 50 ns beam in a circular lattice 11.5 m in circumference. Focusing in the main lattice is provided by 72 printed-circuit (PC), dc powered quadrupoles, while bending is realized with 36 PC dipoles. The air-core magnets are based on double-sided flexible printed circuits where the conducting patterns follow special algorithms (to be introduced below). While this design has many advantages in terms of cost and ease of manufacturing, the small aspect ratio of the magnets, as dictated by stringent space requirements in the ring lattice, has raised concerns about the field quality and the implications for the beam dynamics. Matching experiments in a prototype section employing quadrupoles of an earlier, simplified design [2] have shown that the short lenses perform well over a distance of at least 1 m [3]. A new design with a larger aperture and optimized field characteristics was deemed necessary, however, to better accommodate the relatively large beam cross section of UMER.

While the PC magnets meet the specific demands of our electron ring lattice and beam parameters, the principles behind the design of the printed circuits are valuable to all applications where small fields or gradients can be useful, and simple and cost-effective implementation are important factors. Furthermore, knowledge of the harmonic content of the magnet field and its sources is important for beam dynamics studies as well as for the use of the magnets as steering or correcting elements. An example is the use of the PC quadrupoles as skew elements to correct for beam rotations that result from random rotation errors in the UMER quadrupoles. Although applications of this nature would normally require small dc circuit currents, the PC magnets can be pulsed in situations where higher fields or gradients are needed and heat generation is to be minimized. In fact, to accelerate the UMER beam, the dipoles must be pulsed.

In the next section we present a brief review of the magnet design. This is followed in Sec. III by a description of the rotating coil apparatus. The results of measurements of harmonic content are summarized in the first half of Sec. IV; in the second half, we compare the results to predictions from numerical calculations. These employ models that incorporate different types of magnet errors.

II. MAGNET DESIGN

It is well known that the transverse components of the B field inside a magnet of aperture radius r_0 and far from its ends has the 2D multipole expansion representation

$$B_y + iB_x = \sum_{n=1} (b_n + ia_n)\left(\frac{x + iy}{r_0}\right)^{n-1}, \qquad r = \sqrt{x^2 + y^2} < r_0, \tag{1}$$

where b_n and a_n are the normal and skew $2n$-pole components. In particular, $n = 1$ and $n = 2$ correspond to the dipole and quadrupole terms, respectively. The same

*Permanent address: Institute of Fluid Physics, CAEP, P.O. Box 919-106, Mianyang, Sinchuan 621900, People's Republic of China.

expansion is valid for a magnet of any aspect ratio provided that one interprets B_x and B_y as the axially integrated components of the magnetic field.

In designing a PC magnet we are interested in finding the current distribution over a cylindrical surface that results in an axially integrated transverse field consisting of a single multipole. One can achieve this goal [4,5] by choosing a current density $\vec{K}$ on the cylindrical surface such that its axially integrated longitudinal component $\int K_z\, dz$ has a $\cos n\theta$ azimuthal dependence, with n being the order of the desired multipole. In the UMER magnets the current flow is realized by a single conductor following a rectangular spiral path on the surface of the printed circuit. In first approximation such a current can be represented as following a set of concentric rectangular loops of zero thickness. This is the model we employed in the magnet design. Each loop consists of two pairs of sides: the "active conductors," parallel to the magnet axis, and the "return conductors," perpendicular to the magnet axis (see Fig. 1). Only the current flowing in the active conductors contributes to the axially integrated magnetic field.

Consider the continuum limit where the number of rectangular loops approaches infinity. Also, assume a design in which the azimuthal component of the surface current density K_θ does not depend on z where it is nonvanishing (i.e., on the portion of the cylindrical surface covered by the return conductors). Then it can be shown [5] that the desired density current distribution $\int K_z\, dz \propto \cos n\theta$ is obtained if the semilength z of the active conductors is related to the azimuthal angle θ by

$$z(\theta) = \frac{l}{2}\left[1 - \frac{2k}{n}\,|\sin(n\theta)|\right]^{1/2}, \qquad (2)$$

where $0 \le \theta \le 2\pi$, l is the magnet length, and $k \le n/2$ is an adjustable parameter. An optimal choice that maximizes the desired multipole strength for a given current flow is $k = n/2$.

In a discrete realization of the current flow with a limited number of conductors, one can expect that Eq. (2) would not lead to a perfect single multipole field and therefore should be somehow modified. In the actual design of our magnets we kept Eq. (2) as our guideline, but, in fact, we located the i conductor according to

$$|\sin(n\theta_i)| = 1 - \left(\frac{2z_i}{k'l}\right)^2. \qquad (3)$$

Equation (3) results from rewriting Eq. (2) to show z as the independent variable and using a different adjustable constant k' which is near unity for both the dipoles and the

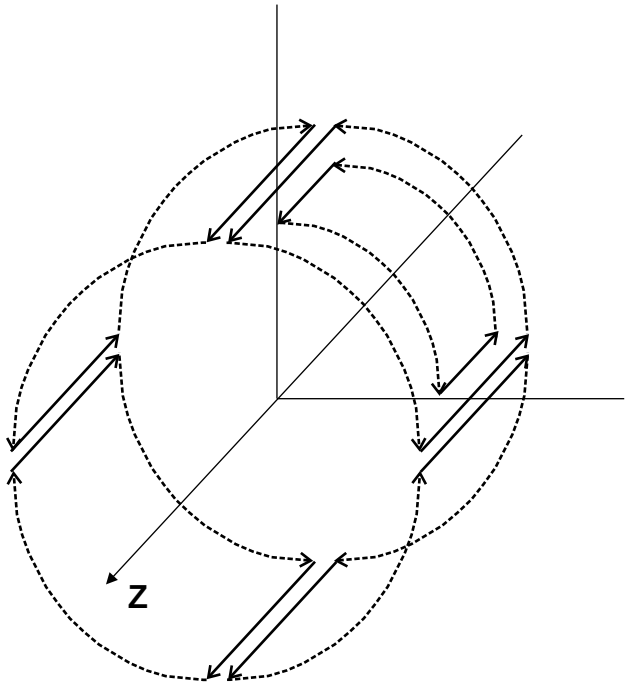

FIG. 1. Basic geometry of conductor layout for modeling printed-circuit magnets. The "active" conductors are shown as solid lines parallel to the beam axis (z axis). The curved dotted lines are the "return" conductors. Current flow is indicated by the arrows.

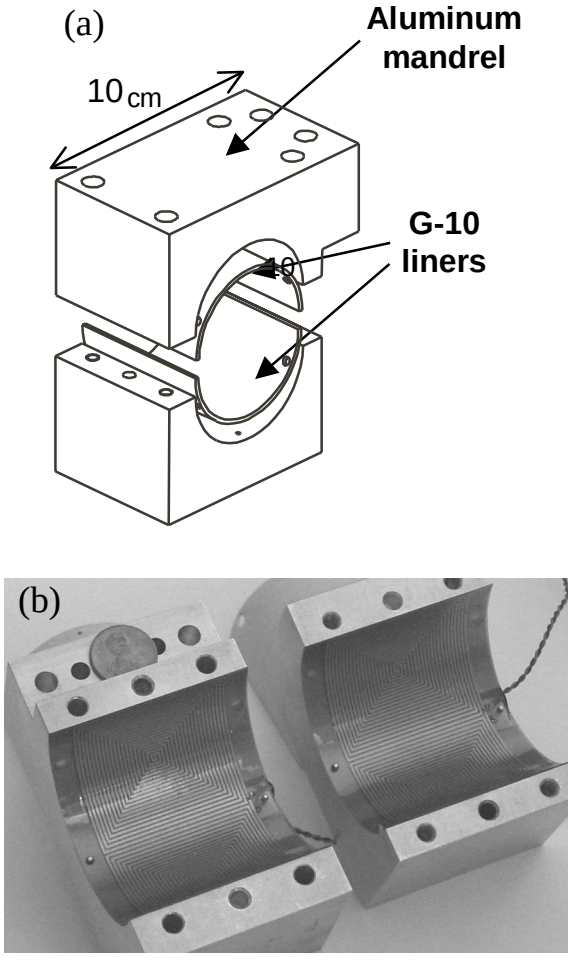

FIG. 2. (a) Exploded view of magnet assembly (the printed circuits are not shown) and (b) photograph of UMER quadrupole halves; the underside of the printed circuits can be seen.

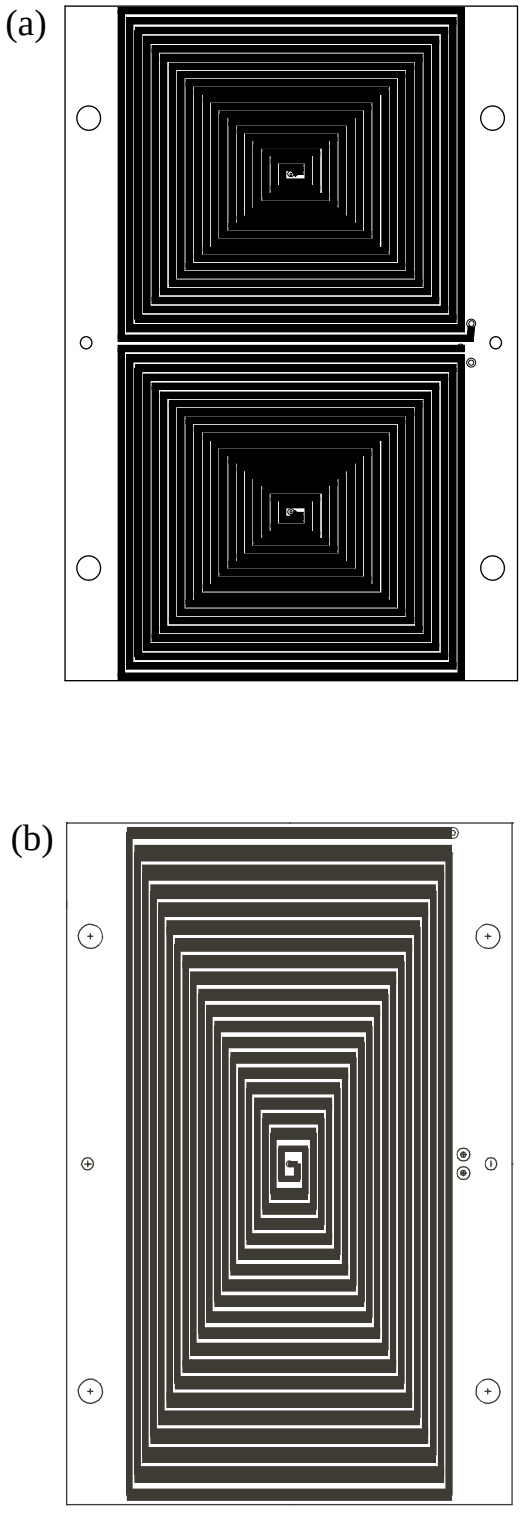

FIG. 3. Upper sides of the double-sided printed circuits that form one-half of the UMER quadrupole magnet (a) and dipole magnet (b) (to scale). The undersides of the circuits have similar patterns, with series connections and opposite rotation so that the fields are doubled and the field due to the external leads is minimized. The small holes near the edges in (a) and (b), in the middle, are used for alignment pins. The bigger holes are used for attaching the circuits to aluminum pieces as shown in Fig. 2(b) for the PC quadrupole.

quadrupoles. The parameter k' was adjusted by optimizing the uniformity of the integrated field (dipole) or the radial linearity of the integrated transverse fields (quadrupole). Equations (2) and (3) are identical with k, or k', set to their ideal values in the continuum limit.

Twenty active conductors per quadrant (dipole) or octant (quadrupole) were chosen. In each quadrant or octant the conductors were located at $z_i = l/2 - i\Delta z$, with $i = 1$ to 20 and $\Delta z = l/42$; Δz is the uniform separation between the return conductors. The adjustable parameter was found to be $k' = 0.976$ for both dipole and quadrupole.

Three features of the UMER magnets are important. First, the construction based on identical halves, as illustrated in Figs. 2(a) and 2(b), enables simple and reproducible assembly and disassembly, so the magnets can be

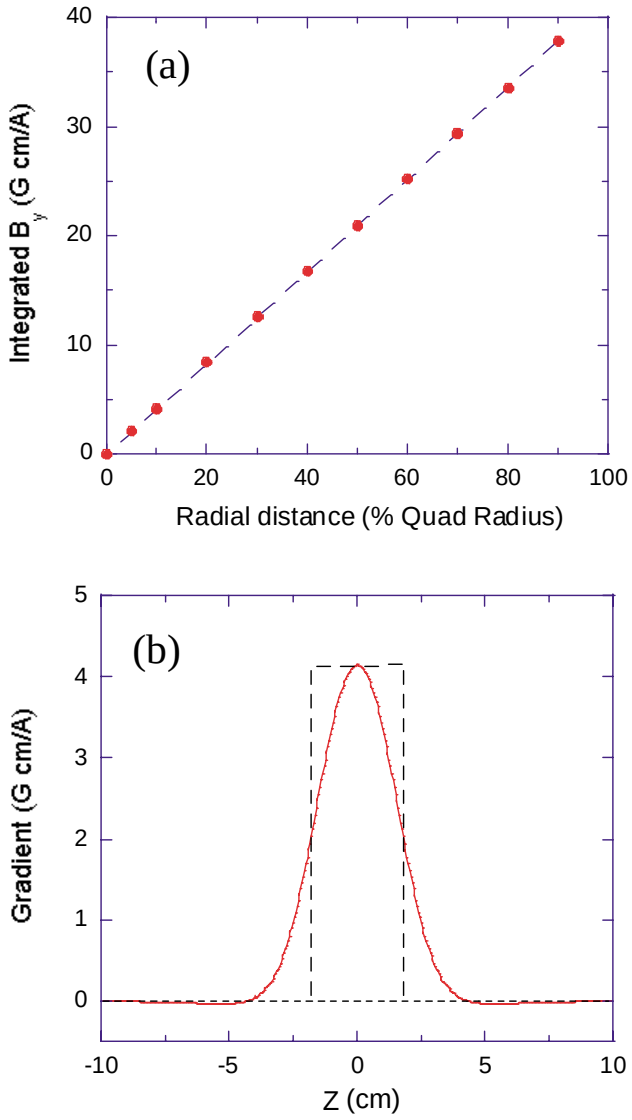

FIG. 4. (Color) Printed circuit quadrupole magnet. (a) Radial variation of axially integrated transverse field, per amp, at $\theta = 0°$, and (b) on-axis gradient profile, per amp. The broken lines in (b) indicate the effective hardtop quadrupole.

TABLE I. Physical and magnetic parameters of PC dipoles and quadrupoles for the UMER.

	Dipole	Quadrupole
Design algorithm	Eq. (3) with $n = 1$	Eq. (3) with $n = 2$
Radius and length (r_0, ℓ)	2.87 cm, 4.44 cm	2.79 cm, 4.65 cm
Aspect ratio (length:diameter)	0.722:1	0.833:1
Conductor location tolerance	± 0.01 cm	± 0.01 cm
Thermal expansion (2 A)	<0.01 cm	<0.01 cm
Avg. resistance at room temperature (2 oz Cu)	1.5 Ω per circuit	3.0 Ω per circuit
Effective length (ℓ_{eff})[a]	3.76 cm	3.63 cm
On-axis peak field per amp (B_0)	5.22 G/A	...
Peak gradient per amp (g_0)	...	4.14 G/cm A
Integrated field per amp	19.6 G cm/A	...
Integrated gradient per amp	...	14.9 G/A

[a] $\ell_{\text{eff}} = \frac{1}{B_0}\int_{-\infty}^{\infty} B(r=0,z)\,dz$, for a dipole magnet, and $l_{\text{eff}} = \frac{1}{g_0}\int_{-\infty}^{\infty} g(r=0,z)\,dz$, for a quadrupole magnet.

removed for bakeout of the transport pipe. Second, a separate, similar design was used for the underside of each printed circuit, with special series connections between the two sides to enable the external connections to be close together. This feature results in near perfect cancellation of the field from the twisted-pair external leads, in addition to doubling the field per ampere. Finally, the same program used to generate the input required for the magnetics program was also used to generate input for a computer-aided design program. This in turn enabled generation of a file to be sent directly to the printed-circuit manufacturer.

The conductor geometries of the upper side layers of half-quadrupole and half-dipole printed circuits are shown in Figs. 3(a) and 3(b), respectively. The radial variation of the axially integrated transverse field (per amp) of the PC quadrupole and the on-axis gradient (per amp) are shown in Figs. 4(a) and 4(b), respectively.

Table I summarizes the physical parameters and field properties of the UMER PC quadrupole and bend dipole. The parameters in the last five rows are the results of calculations based on a rectangular-loop geometry, with the iron-free magnetics program MAG-PC [6]. One could compare these numbers with the integrated on-axis magnetic field $\overline{b}_1$ (for the dipole) and integrated field gradient $\overline{b}_2/r_0$ (for the quadrupole) given by

$$\overline{b}_1 = \frac{\mu_0}{8}\,\frac{l^2 I}{r_0 \Delta z}\,, \tag{4}$$

$$\frac{\overline{b}_2}{r_0} = \frac{\mu_0}{4}\,\frac{l^2 I}{r_0^2 \Delta z}\,. \tag{5}$$

The two formulas above are obtained from the continuous current density model by assuming that one can approximate $K_\theta \simeq I/\Delta z$, where I is the current in each circuit loop in the discrete model. Equations (4) and (5) yield 19.9 G cm/A, and 14.7 G cm/A, i.e., values about 1% different from those of Table I. These deviations are a measure of the accuracy of a modeling based on the assumption of a continuous surface density current.

We conclude this section with a few remarks. The first is that the symmetry involved in the placement of the conductors automatically excludes the appearance of some terms in the multipole expansion (at least as long as the conductors are infinitesimally thin). In particular, for a dipole and quadrupole one can show that the "allowed" multipoles are, respectively, $n = 2m + 1$ and $n = 4m + 2$, with $m = 0, 1, 2, \ldots$.

The second is that the representation of the current flow in terms of concentric rectangular loops is also an approximation. We found that the deviation between the main multipole field components as calculated using this model and the actual spiral geometry is of the order of 0.1%. Field calculations based on the latter model will be discussed in Sec. IV.

Finally, we want to emphasize that the 2D expansion (1) does not apply in the magnet end regions where the longitudinal component of the B field is nonvanishing. In fact, it would provide a very poor representation of the B field of our magnets because of their short aspect ratio. As already pointed out, Eq. (1) can be applied only to the axial integrals of the magnetic field components. A full 3D field representation would reveal the existence of some additional terms that in the literature are often referred to as "pseudomultipoles." They carry some extra nonlinearities in the beam dynamics that cannot be avoided. These nonlinearities were a concern at the initial stage of the UMER design. However, beam dynamics simulations [5,7,8] have shown that their presence is not detrimental to the machine performance.

III. ROTATING COIL MAGNETOMETER

An accurate, widely used method for determining the field quality of magnets used in accelerators is the rotating coil [9]. Special designs are commonly used for measurements of particular multipole components of the magnet field [10]. A simpler alternative consists of a rectangular coil spinning so that one side of the coil is positioned along the axis of the magnet. The coil is attached to a

motor and spun at 6 ± 0.001 Hz. The induced voltage is then fast-Fourier transformed (FFT) electronically to get information on the harmonic content of the magnet field. The phase of rotation of the coil can be obtained by using an optomechanical synchronous signal to trigger the scope. The signal is derived from a photogate circuit that operates with the passage of a 0.76 ± 0.025 mm slot when the rotation angle is 90° ± 0.1° relative to the horizontal plane of the magnet. To shield the effect of the Earth's field, a mu-metal box is employed that reduces the field to about 5 mG at the coil.

A schematic of the rotating coil setup is shown in Fig. 5(a). The coil used to characterize the PC quadrupoles and dipoles for UMER has effective dimensions $R = 2.22$ cm by $l_c = 12.7$ cm [see Fig. 5(b)]. It is fabricated by winding about 3000 turns of very fine 44-gauge copper wire on a plastic spool [11]. Nonmagnetic (either brass or stainless steel 316L) screws and alignment pins are used throughout the structure, but the stages for vertical and horizontal adjustments [along "y" and "x" in Fig. 5(a)] are made of slightly magnetic steel. The three-axis support system is fitted with nonmagnetic micrometer screws that permit pitch, yaw, and roll adjustments with a resolution of about 0.05°. The printed-circuit halves that form a magnet are mounted on the underside of aluminum mandrels [Fig. 2(b)] with the help of plastic (G-10) semicircular liner shells and alignment pins. The aluminum mandrels are constructed with high tolerances (on the order of 0.025 mm), and are relatively heavy so they can function well as heat sinks.

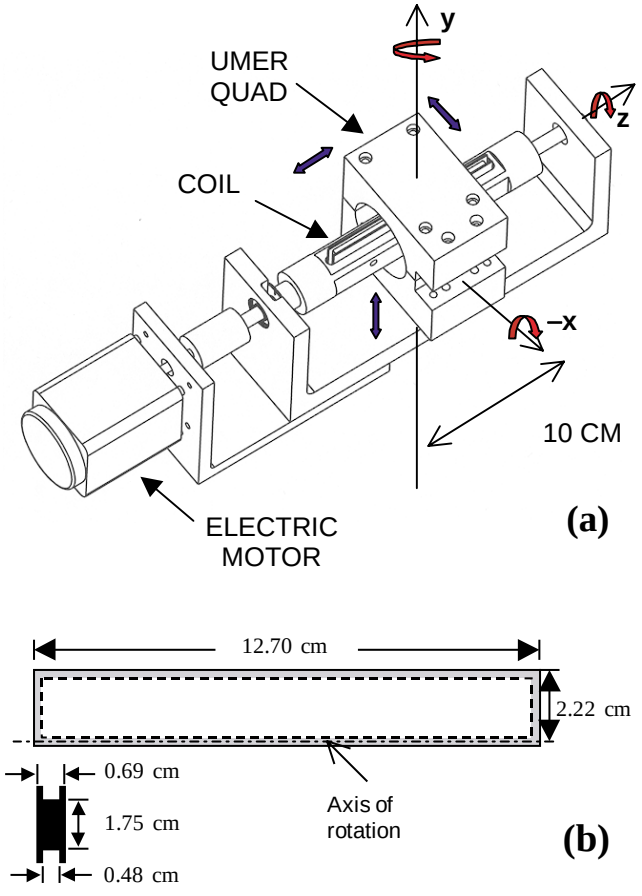

FIG. 5. (Color) (a) Schematic of rotating coil apparatus. The magnet mount is attached to plates not shown in the drawing. (b) Coil dimensions. In (a), the solid arrows indicate the possible adjustments of the magnet relative to the coil. The whole of the rotating coil apparatus is normally enclosed in a mu-metal box.

The induced emf per loop in the rotating coil can be written as

$$\varepsilon(t) = \sum_{n=1} \varepsilon_{bn} \sin(n\omega t) + \varepsilon_{an} \cos(n\omega t), \qquad (6)$$

where ϵ_{bn} and ϵ_{an} are associated with the normal and skew coefficients in Eq. (1). Explicitly, the voltage amplitude for the normal part is easily obtained by integrating the azimuthal component of the B field over the plane of the coil,

$$\varepsilon_{bn} = l_c \omega \overline{b}_n \frac{R^n}{r_0^{n-1}}, \qquad \overline{b}_n = \frac{1}{l_c} \int_{-l_c/2}^{l_c/2} b_n(z)\, dz, \qquad (7)$$

where l_c is the coil's length, $R = 0.73 r_0$ is the coil's height in terms of the aperture radius of the magnet, and ω is the angular frequency of rotation of the coil. As an example, we compute the amplitude signal from the main multipole term of the UMER quadrupole magnet: by approximating $l_c \overline{b}_2 \approx l_{\text{eff}} g_0 r_0$ and using data from Table I (where the effective length l_{eff} is defined), we find $\epsilon_{b2} = 23\ \mu$V/A turn, or about 140 mV for the 3000-turns rotating coil and 2 A on the PC quadrupole magnet. This voltage translates into an FFT peak on the scope given by $20 \log(140/316)$ dBm $= -7.1$ dBm, in good agreement with measurements (see next section). Similarly, for the PC dipole magnet we find $\epsilon_{b1} = 15.5\ \mu$V/A turn, which corresponds to a FFT peak of -10.6 dBm, again very close to measurement. Unfortunately, similar simple calculations are not possible for the higher harmonics, although exact analytical expressions can be written for the coefficients $\bar{b}_n, \overline{a}_n$ in the framework of a concentric-loop model for the conductor pattern [5].

IV. SPATIAL HARMONICS

A. Measurements

Table II shows the results for the normal and skew multipole components after averaging over spectra for eight PC dipoles or quadrupoles. In the table, $\overline{B}_n \equiv (\overline{b}_n/\overline{b}_1) \times 10^4$, $\overline{A}_n \equiv (\overline{a}_n/\overline{b}_1) \times 10^4$ for the dipole magnet, and $\overline{B}_n \equiv (\overline{b}_n/\overline{b}_2) \times 10^4$, $\overline{A}_n \equiv (\overline{a}_n/\overline{b}_2) \times 10^4$ for the quadrupole magnet. As is customary, the values of the dimensionless multipole coefficients are given such that the normal component of the main harmonic is equal to 10^4.

The synchronous signal mentioned above, together with the rotating coil signal for a quadrupole magnet, is

TABLE II. Average normal ($\overline{B}_n$) and skew ($\overline{A}_n$) integrated multipole components, and associated errors, of PC dipoles and quadrupoles in UMER.

	PC dipole magnet ($R = 0.71r_0$)				PC quadrupole magnet ($R = 0.73r_0$)			
n	$\overline{B}_n$	σ	$\overline{A}_n$	σ	$\overline{B}_n$	σ	$\overline{A}_n$	σ
1	10^4	0.19	−0.26	15	−2.0	10	8.6	4.8
2	−4.1	18	3.4	8.0	10^4	0.83	16	36
3	−35	6.9	26	4.3	−32	24	32	12
4	20	10	29	8.6	53	15	54	6.3
5	−100	6.2	−31	8.1	−4.8	22	9.7	13
6	−25	17	−33	8.5	3.2	18	−37	10

illustrated in Fig. 6. The normal and skew components are obtained from the discrete Fourier transform of the average voltage waveform taken over 512 rotating coil cycles, each signal being obtained at 100 kilosamples/s. Initially, nonzero skew components for the main multipoles are observed. The $n = 2$ skew component of the quadrupole magnet ($\epsilon_{a2}/\epsilon_{b2} = -0.0238$, before correction) is about twice the $n = 1$ skew component of the dipole magnet ($\epsilon_{a1}/\epsilon_{b1} = -0.0127$, before correction), pointing to a simple connection to the angular error introduced by the slot used to produce the scope trigger signal. Thus, we derive the angle error for the dipole's main component and use it to correct all normal and skew components for both dipole and quadrupole magnets. This amounts to setting the y axis along the direction of the dipole magnetic field.

A direct observation of the magnitude spectrum is useful during initial alignment of the magnet mount relative to the coil. Adjustments in the transverse directions are done until the dipole component in the FFT spectrum is as close as possible to the peak observed when only the mu-metal shielded Earth's field is present, i.e., about −60 dBm, as in Fig. 7(a). Figures 7(b) and 7(c) show typical multipole spectra for the PC dipole and quadrupole magnets, respectively, when operated at 2 A. Typically, a quadrupole mount must be displaced about $\Delta x = 0.15$ mm to obtain a FFT dipole peak as in Fig. 7(a). From Eq. (7), $\epsilon_{b1} \approx l_{\text{eff}} R g_0 \Delta x$ per turn, or −50 dBm, in close agreement with the dipole FFT component measured *before* alignment.

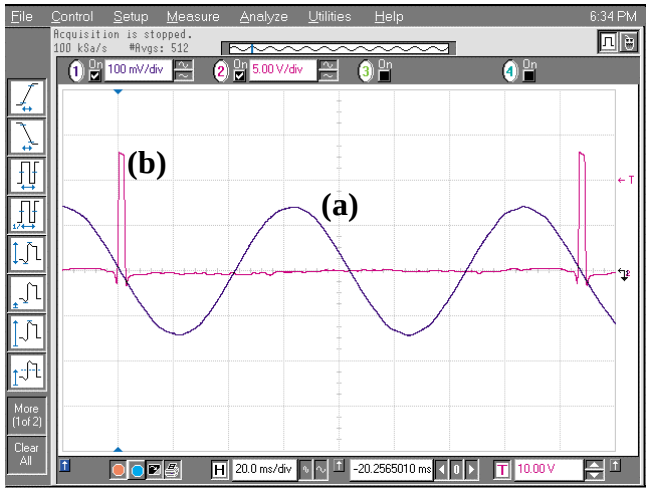

FIG. 6. (Color) Scope signals from rotating coil. (a) PC quadrupole (100 mV/div) and (b) synchronous signal (5.00 V/div) from photogate circuit. The horizontal scale is 20 ms/div.

From Table II, the measured "forbidden" harmonics show significantly greater variability than the allowed ones: among the former, the quadrupole ($n = 2$) and octupole ($n = 4$) terms in the case of the dipole magnet, and the sextupole ($n = 3$) and decapole ($n = 5$) terms for the quadrupole magnet. The only allowed term with a large relative error is the normal duodecapole for the quadrupole magnet—errors that are bigger than the measured quantities result from changes in sign in the original normal and skew components for eight magnets. These observations illustrate the difficulties of harmonics measurement with small fields. Therefore, we emphasize that the tabulated values do not reflect peculiarities of the printed-circuit design alone but include the whole of the magnet assembly and mounting on the rotating coil apparatus. Naturally, we expect that these conditions are representative of those in the ring lattice. In the next section we compare the results presented with predictions from theory and computer calculations that incorporate errors from different sources.

When the numbers in Table II are compared with results for more standard (i.e., "long") dipoles and quadrupole magnets, we find that our values are roughly comparable to what is measured at the ends of those magnets [12]. In turn, these "end" multipoles are normally much larger than the "body" multipoles, i.e., the multipoles measured near the magnet center. In our case, however, the body multipoles are not meaningful since the axial field profiles have no "flattop" [see Fig. 4(b)]. Furthermore, particle-in-cell simulations of the beam dynamics in UMER [13] using multipole strengths close to those reported here indicate acceptable emittance growth over about 100 turns. This small number of turns makes it unnecessary to include multipoles beyond $n = 6$.

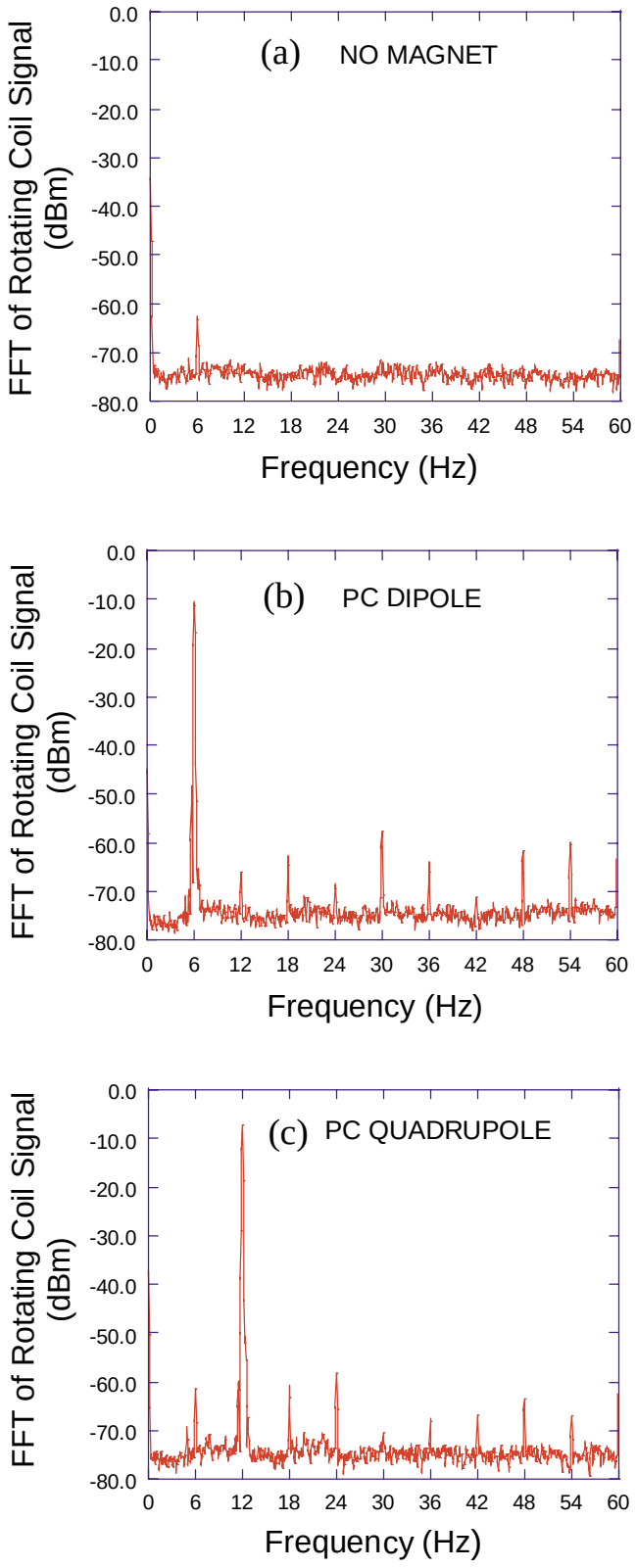

FIG. 7. (Color) Fast-Fourier transform signal from digital scope with (a) no current on the PC magnet, and mu-metal shield present, (b) powered PC dipole magnet (2 A), and (c) powered PC quadrupole magnet (2 A). The rotating coil spins at 6 ± 0.001 Hz; the FFT is calculated every 10 s and the average over 5 min is displayed.

Other effects that were investigated are the possible distortions of the printed circuits from the heat generated or from the use of thicker conductor patterns. For the nominal 2 oz copper printed circuits, no significant changes in the harmonic content up to $n = 6$ were observed, as evidenced by a linearity check on powering up (to 3.0 A) and powering down the magnets. When 3 oz Cu PC quadrupoles were used, on the other hand, the heat generated for the same current was significantly reduced, but, interestingly, the magnitudes of the sextupole and decapole harmonics were doubled, leaving the other multipoles unchanged. An interpretation of this result is deferred to the next section.

B. Calculations

Analytical [5] and numerical calculations using a rectangular loop model for the conductor pattern on the printed circuits yield, as expected, only normal components for the harmonics spectra of the magnet fields. Further, in the absence of assembly or alignment errors, only the harmonics predicted from simple symmetry considerations (see Sec. II) are obtained.

The numerical calculations involve the integration of the Biot-Savart law for the conductor geometry. Each active or return conductor in the specification file written for the iron-free magnetics code MAG-PC is divided into up to 40 segments, so the field components from each current element (about 0.5 mm long) can be easily calculated. The code is run with 8-digit accuracy to evaluate the magnetic field components at 128 uniformly spaced azimuth angles at a radius equal to the effective radius of the rotating coil. Additional programs are used to integrate the transverse fields over the length of the rotating coil (0.5 mm integration step) and, from the results, to calculate the discrete Fourier transform.

When the PC conductor layout is modeled with the *spiral* geometry of the top conductor layer in the actual circuits [see Figs. 3(a) and 3(b)], calculations show the appearance of new forbidden multipoles. The lowest order new component for the quadrupole magnet is a normal octupole of about 0.13%; for the dipole magnet, the lowest order is a normal quadrupole of about 0.33%. In Table III we summarize the results of MAG-PC calculations, with and without errors in the quadrupole magnet. Three types of plausible errors are considered: horizontal and vertical relative displacements of the two magnet halves and edge rotation of one magnet half. The type of error denoted "H" in Table III corresponds to opposite *horizontal* displacements of the magnet halves by 0.1 mm along the x axis [see Figs. 5(a) and 8(a)]. Similarly, error "V" [Fig. 8(b)] is a symmetrical *vertical* separation of the two magnet halves (along the y axis), also by 0.1 mm, for a total gap of 0.2 mm. Error "R" is a *rotation* of the upper magnet half by 0.1° about an axis parallel to and on the farthest edge of the mount [Fig. 8(c)]. The values 0.1 mm and 0.1° used for the different errors are estimated from the mechanical

TABLE III. Results of MAG-PC calculations for UMER quadrupole magnets. The types of errors implemented are explained in the text and illustrated in Fig. 8.

	Without magnet errors				With magnet errors							
	Rectangle		Spiral		H		V		R		HVR	
n	$\overline{B}_n$	$\overline{A}_n$	$\overline{B}_n$	$\overline{A}_n$	$\overline{B}_n$	$\overline{A}_n$	$\overline{B}_n$	$\overline{A}_n$	$\overline{B}_n$	$\overline{A}_n$	$\overline{B}_n$	$\overline{A}_n$
1	0	0	0	0	0	0	0	0	3.8	−8.7	3.8	−8.7
2	10^4	0	10^4	−0.41	10^4	55	10^4	−0.41	10^4	−18	10^4	38
3	0	0	0	0	0	0	0	0	−20	0.10	−20	0.21
4	0	0	−13	0.02	−13	44	−57	0.02	−24	0.16	−68	45
5	0	0	0	0	0	0	0	0	−13	0.44	−13	0.61
6	5.1	0	−76	0	−78	41	−120	0	−88	0.53	−130	43

tolerance of the magnet mounts and errors from magnet assembly and alignment in the rotating coil apparatus.

The appearance of small numerical skew components in two cases ("Spiral" and V in Table III) may point to limitations in the accuracy of the code. The double integration required for the calculations (Biot-Savart law and axial integration) may entail numerical error propagation larger than anticipated. However, the largest skew component in the two columns is only 0.004% of the main term. Moreover, the calculation results for the two geometries (i.e., rectangular loops and spiral) when no magnet errors are included agree with analytical results, so the code is deemed reliable for the situations when magnet errors are implemented.

The calculations with magnet errors are based on a spiral conductor geometry. For comparison, the same errors were implemented in a geometry based on rectangular loops, but the results are not included here. The comparison between the two geometries reveals that the normal octupole component of the quadrupole magnet is due to error V (0.57%) and, to a lesser extent, the spiral geometry (0.13%). The skew octupole, on the other hand, is accounted for by error H (0.44%). The appearance of skew quadrupole (0.55%) and duodecapole (0.41%) terms is also related to error H. A normal duodecapole term is associated with the spiral geometry (0.76%) and the design. Error V (0.39% rectangular loops, 1.20% spiral) also contributes to the normal duodecapole. Finally, the type of error that produces the richest spectrum is R in either geometry: normal sextupole (0.20%) and decapole (0.13%).

When the three types of magnet errors are combined in MAG-PC, the results, shown in the two columns under "HVR," are in most cases just the sum of the separate contributions. No attempt is made, however, to "fit" the measured harmonics presented in Table II by combining the magnet errors with different weights, since a close examination of Tables II and III already shows a fair agreement. The most likely sources of the different measured harmonics for the PC quadrupole magnets are summarized in Table IV.

To understand the occurrence of skew sextupole and decapole harmonics (Table II), we have to invoke errors other than the ones tabulated. A simple calculation shows that the finite width of the conductors gives rise to small *skew* components of all multipoles. Furthermore, MAG-PC calculations where the radial locations of conductors are

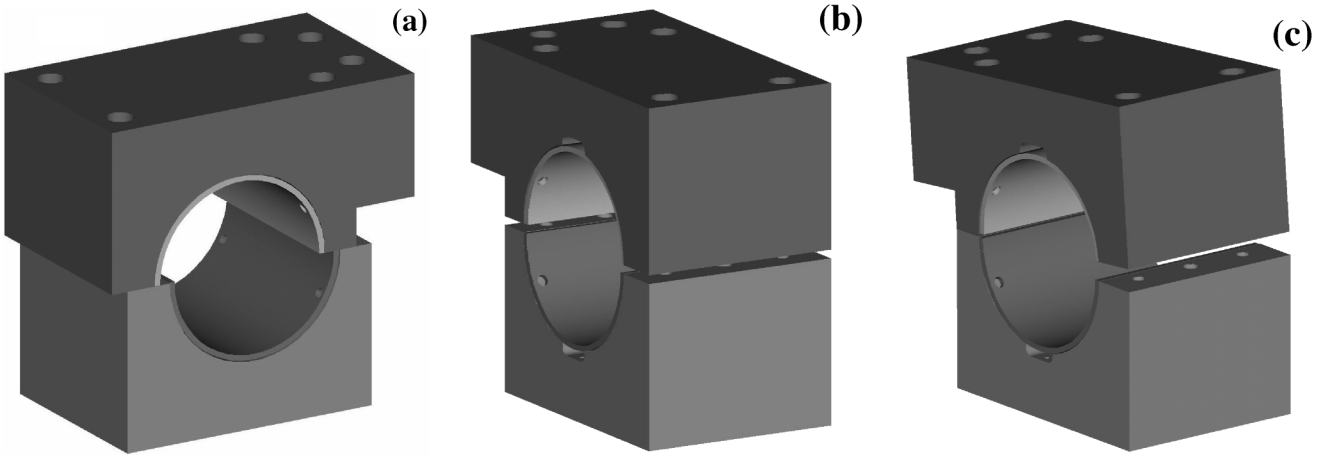

FIG. 8. Magnet errors implemented in MAG-PC for calculations of multipole content. (a) Symmetrical horizontal shift of magnet halves, (b) symmetrical vertical shift of magnet halves, and (c) edge rotation of upper magnet half. The errors are greatly exaggerated in the figures.

TABLE IV. Sources of PC quadrupole multipole spectrum (see Tables II and III).

Multipole	Source
Normal dipole	Residual Earth's field and *R*
Skew dipole	Residual Earth's field and *R*
Normal quadrupole	Design
Skew quadrupole	H and R
Normal sextupole, decapole	R
Skew sextupole, decapole	Conductor finite width
Normal octupole	V
Skew octupole	H
Normal duodecapole	Design and V
Skew duodecapole	H

modified (by ± 0.1 mm) to simulate a "ripple" in the printed-circuit surface also display skew sextupole and decapole terms of the same order of magnitude as the observed ones. The fact, mentioned before, that 3 oz copper quadrupoles display sextupole and decapole terms that are about twice those of the nominal 2 oz copper quadrupoles seems to corroborate the role of magnet deviation from circular cross section: thicker conductors make the printed-circuit stiffer and harder to conform to the mount shape. Finally, other likely sources reside in the rotating coil apparatus itself, e.g., the field distortions caused by the slight magnetism present in some components, or the finite width of the coil winding. Regarding the latter, we point out that the largest loops in the coil winding extend beyond the rotation axis, so some multipoles are enhanced: dipole, sextupole, and decapole terms, as for a coaxial rotating coil.

Calculations for the PC dipole magnet, including magnet errors as in Table III, do not agree with measurements as well as for the PC quadrupole case. An important difference between the two designs, though, is the width of the *active* conductors. As seen in Figs. 3(a) and 3(b), the PC dipole has almost the same overall dimensions as the PC quadrupole but half the number of active conductors per circuit, so the conductor width is about twice that for the PC quadrupoles. The width of the return conductors, on the other hand, is almost the same in both cases. Thus, modeling the dipole magnet by assuming a current flow through the conductor middle lines may not be accurate enough, not to mention the possible effects of a varying cross section along the active conductor paths. A possible remedy is to model the wide active conductors as pairs of thin conductors around the middle lines, with each thin conductor carrying half the current.

An extension of this work will include refinements of the rotating coil apparatus to reduce the residual magnetism, improved resolution of pitch, yaw, and roll adjustments, and, possibly, the addition of a fixture coaxial with the coil for direct mounting of the printed circuits. This last feature would allow for multipole measurements unaffected by the errors in the assembly of the magnet halves.

V. SUMMARY AND CONCLUSIONS

We have presented general formulas useful for the design of air-core printed-circuit magnets and illustrated their use with the bending and focusing magnets of the UMER. The integrated field of the dipole and integrated gradient of the quadrupole magnets can be estimated in the framework of a continuous current distribution. The results are adequate for general calculations in a lattice, e.g., bending or steering and rms envelope matching.

For a detailed characterization of the PC magnets, however, knowledge of their multipole spectrum is necessary. Since the peak magnetic fields involved are as small as 15 G, we have designed a special rotating coil magnetometer that uses mostly nonmagnetic components and mu-metal shielding. Furthermore, a synchronous signal allows for the determination of normal and skew components. For the calculations, an iron-free magnetics computer program permits simple implementation of plausible magnet errors. A combination of these errors, which arise mostly from assembly of the magnet halves, yields multipole spectra that are in fair agreement with measurements for the PC quadrupole.

ACKNOWLEDGMENTS

We thank J. G. Wang and D. Sutter for useful discussions, Paul Chin for assistance with mechanical design and construction, and D. Brosius and M. Virgo for help with LateX. This work is supported by the U.S. Department of Energy.

[1] M. Reiser *et al.,* Fusion Eng. Des. **32-33**, 293 (1996). See also M. Reiser, *et al.,* in *Proceedings of the 1999 Particle Accelerator Conference, New York* (IEEE, Piscataway, NJ, 1999), p. 235.
[2] T. F. Godlove, S. Bernal, and M. Reiser, in *Proceedings of the 1995 Particle Accelerator Conference, Dallas, Texas* (IEEE, Piscataway, NJ, 1996), p. 2117.
[3] S. Bernal *et al.,* Phys. Rev. ST Accel. Beams **1**, 044202 (1998).
[4] Robert T. Avery, Glen R. Lamberston, and Chester D. Pike, in *Proceedings of the 1971 Particle Accelerator Conference, Chicago* (IEEE, Piscataway, NJ, 1971), p. 885.
[5] M. Venturini, Ph.D. thesis, University of Maryland, 1998.
[6] Infolytica Corporation, Montreal, Canada.
[7] M. Venturini, S. Bernal, A. Dragt, M. Reiser, J. G. Wang, and T. Godlove, Fusion Eng. Des. **32-33**, 283 (1996)
[8] R. Kishek, *et al.,* in Proceedings of the International Computational Accelerator Conference (ICAPS), 1998, Monterey, CA (to be published).
[9] W. G. Davies, Nucl. Instrum. Methods Phys. Res., Sect. A **311**, 399 (1992).
[10] G. H. Morgan, in *Proceedings of the International Conference on Magnet Technology, 1972,* edited by Y. Winterbottom (U.S. Dept. of Com., Washngton, DC, 1972), p. 787.

[11] Rawson-Lush Instrument Co., Acton, Massachusetts.
[12] See, for example, J. Wei *et al.,* in *Proceedings of the 1998 European Particle Accelerator Conference, Stockholm, Sweden* (Institute of Physics, Bristol, UK, 1998), p. 380.
[13] R. Kishek, M. Reiser, P. G. O'Shea, M. Venturini, and W. W. Zhang (to be published).